Science Advances
AAAS

Supplementary Materials for

Theory of defect-mediated morphogenesis

Ludwig A. Hoffmann, Livio Nicola Carenza, Julia Eckert, Luca Giomi*

*Corresponding author. Email: giomi@lorentz.leidenuniv.nl

Published 15 April 2022, *Sci. Adv.* **8**, eabk2712 (2022)
DOI: 10.1126/sciadv.abk2712

The PDF file includes:

Other Supplementary Material for this manuscript includes the following:

I. EXPERIMENTAL DETAILS.

Cell culture. Parental Madin-Darby Canine Kidney (MDCK) GII cells (kindly provided by M. Gloerich, UMC Utrecht) were cultured in a 1:1 ratio of low glucose DMEM (D6046; Sigma-Aldrich) and Nutrient Mixture F-12 Ham (N4888; Sigma-Aldrich) supplemented with 10% fetal calf serum (Thermo Fisher Scientific), and 100 mg/mL penicillin/streptomycin, 37 °C, 5% CO_2. For experiments, cells were seeded on non-coated cover glasses and cultured in high-glucose Dulbecco Modified Eagle's Medium (D1145; Sigma-Aldrich) supplemented with 10% fetal calf serum, 2 mM glutamine, and 100 mg/mL penicillin/streptomycin. Before fixation, cells were incubated for 2 h in the CDK1-inhibitor RO-3306 (10 μM in final concentration; SML0569; Sigma-Aldrich).

Immunostaining. After 8 h, cells formed a closed monolayer. To increase the cell density within the monolayer and to attain a buckling instability, cells were cultured for a total of 25 h and then fixed for 15 min in 4% paraformaldehyde (43368; Alfa Aesar) in phosphate-buffered saline (PBS). After fixation, cells were permeabilized for 10 min with 0.1% Triton-X 100 and blocked for 60 min with 1% bovine serum albumin in PBS. E-cadherin was visualized using an E-cadherin rabbit antibody (1:500 ratio; 24E10; Cell Signalling) followed by staining with Alexa 532 antirabbit secondary antibody (1:500 ratio; A-11009; Invitrogen). F-actin was stained with Alexa Fluor 647-labeled phalloidin (1:500 ratio; A22287; Invitrogen) and the DNA with DAPI (1:1000 ratio; Sigma- Aldrich).

Microscopy. Samples were imaged at high resolution on a home-build optical microscope setup based on an inverted Axiovert200 microscope body (Carl Zeiss, Oberkochen, Germany), a spinning disk unit (CSU-X1; Yokogawa Electric, Musashino, Tokyo, Japan), and an emCCD camera (iXon 897; Andor Labs, Morrisville, NC). IQ-software (Andor Labs) was used for setup-control and data acquisition. Illumination was performed using fiber-coupling of different lasers (405 nm (CrystaLaser, Reno, NV), 514 nm (Cobolt AB, Solna, Sweden), and 642 nm (Spectra-Physics Excelsior; Spectra-Physics, Stahnsdorf, Germany)). Cells adhered on a cover glass were inspected with an EC Plan-NEOFLUAR 40 1.3 Oil Immersion Objective (Carl Zeiss).

Image analysis. Cell segmentations and the height-to-radius profile analysis were performed using written scripts in Matlab2018a. Cell boundaries were identified from a maximum intensity projection of the F-actin signal of a confocal z-stack of the top part of the dome. The height profile was determined by the averaged intensity of the F-actin signal of a radius-dependent annulus area per plane of the z-stack. Fiji software was used for the orthogonal view of the dome. 3D reconstructions were done by ImarisViewer9.7.0 and z-directions were corrected for spherical aberration and axial distortion [56].

II. HEIGHT FUNCTION OF MDCK DOMES

MDCK GII epithelial cells were growing on a coverslip. We observe that, after they formed a closed monolayer on the substrate, non-planar features, so called domes, developed due to the superelastic properties of the cells [22]. We imaged domes of different heights and diameters (see Fig. 1). Depending on the focal plane between the inner and outer area of the monolayer, cells changed their cell-cell contact length and the number of nearest neighbors. As described in the main text, this leads to the presence of topological defects in regions of high curvature (Fig. 1A and B). Furthermore, we sometimes found the additional disordered and folded structures on top of domes, see for example Fig. 1C. We measured the height of the buckled cell layer above the flat substrate. The height-to-radius profile of the outer area of the monolayer shows with increasing radius an increase in height, see Fig. 1D. We assume that the buckling instability and the formation of additional structures on top of the dome is caused by the cells continued division and growth even after they form a closed monolayer. The growth and division would cause the buildup of stresses in the monolayer that are relieved by the buckling. This is in agreement with e.g. Ref. [6]. We

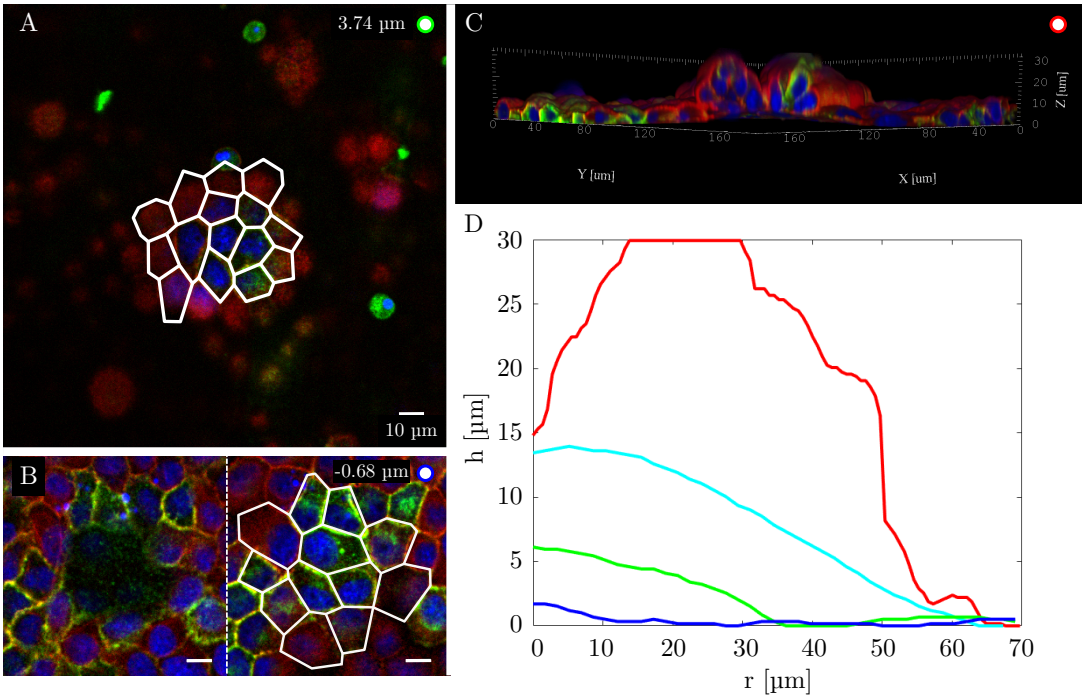

Figure 1. **Domes in MDCK layers.** Pictures of three domes of different sizes in panels (A)-(C) for which we measured the height of the cell monolayer above the flat substrate. The height of the outer area of domes as a function of the radius (distance from the center of the dome along the flat reference plane) is shown in panel (D). The color of each plot corresponds to the label in the panels (A)-(C), cyan to the dome in Fig. 1D in the main text. Segmented cells of domes shown in panel (A) and (B) illustrate the presence of topological defects near the top of the dome. For the three smallest domes, namely the functions colored blue [shown in panel (B)], green [shown in panel (A)], and cyan (shown in Fig 1D in the main text), we see that with increasing height at the center both the radius of the dome and the width of the plateau of constant height near the center are increasing. Furthermore, the height is a monotonically decreasing function of the radius. Instead, for the largest dome [red and shown in panel (D)] additional chaotic and folded structures were observed on top of the dome such that the height is maximal away from the origin. Red: F-actin, green: E-cadherin, blue: nuclei.

speculate that, consistently with the mechanism outlined in the main text, a net positive topological charge could facilitate the out-of-plane deformation of the monolayer, hence the formation of domes, in combination with other system-specific mechanisms, such as the injection of fluid under the cell layer which results in a focal detachment [21, 22]. Furthermore, it is possible that a difference in ion-concentration surrounding the monolayer between apical and basal side can even support the dome formation in areas where topological defects appear, see also Ref. [21].

To support this speculation, we have we analyzed eleven domes and counted the total topological charge in the central region, where the Gaussian curvature is maximal and positive. The topological charge of a cell having c_i sides is conventionally defined as $q_i = 6 - c_i$. Thus, pentagonal cells (i.e. $c_i = 5$) have topological charge $q_i = 1$, whereas heptagonal cells (i.e. $c_i = 7$) has charge $q_i = -1$. The total topological charge is then computed by summing the individual charges of all the cells in the central region of a dome, hereafter referred to as "region of interest" (ROI): $Q = \sum_{i \in \mathrm{ROI}} q_i$ (see Fig. 2A). We found that all domes in our sample feature a positive total topological defect charge, with the mean charge of the eleven domes being $Q_{\mathrm{mean}} = 9.3 \pm 4.9$ (mean $\pm$ standard deviation).

Furthermore, as shown in Fig. 2B we find that the total topological charge of a dome is strongly correlated with the total number of cells per dome (linear correlation coefficient $r = 0.85$). Such a linear relation, is consistent with the hypothesis that the topological charge of the cellular monolayer effectively screened by its Gaussian curvature, i.e.

$$Q \approx \int_{\mathrm{dome}} \mathrm{d}A\, K\,. \tag{1}$$

To illustrate this point, one can approximate the dome as a spherical cap of radius R, so that $K = 1/R^2$ and $\mathrm{d}A = \mathrm{d}\Omega\, R^2$, with $\mathrm{d}\Omega$ the infinitesimal solid angle. The right hand side of Eq. (1) equates then the solid angle $\Delta\Omega$ spanned by the ROI: i.e. $Q \approx \Delta\Omega$ (see Fig. 2A). This, in turn, is proportional to the number of cells it encloses, given

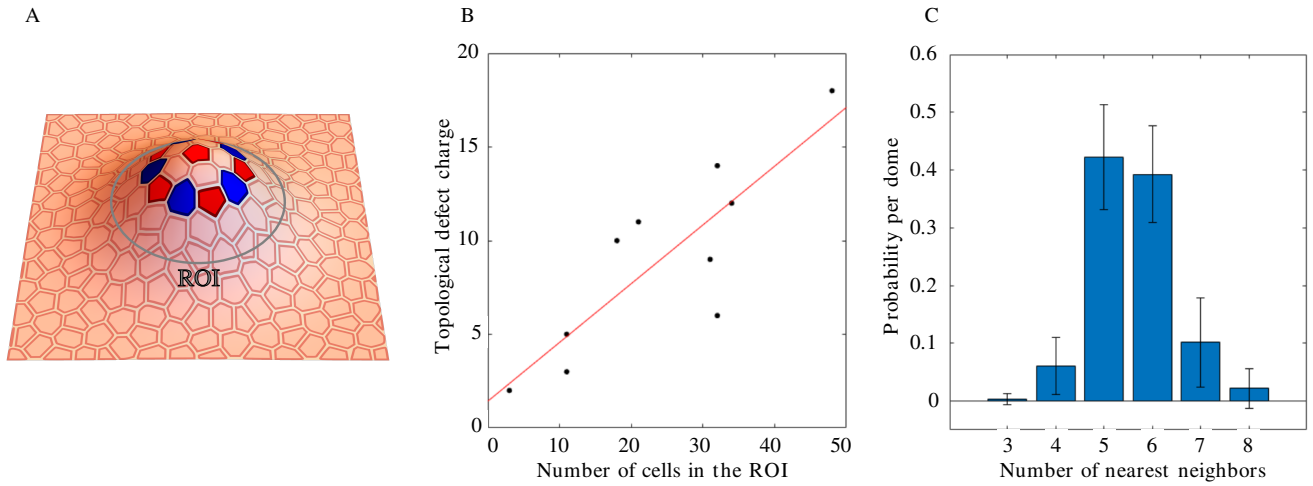

Figure 2. **Topological charge of domes.** (A) Sketch of topological defects on a dome. Heptagons are blue and pentagons are red. (B) The total topological defect charge per dome increases linearly with the number of cells constituting the dome. (C) The cells contributing a positive topological charge are mainly pentagons. The height of each bar in the histogram is the averaged probability of finding a cell with n nearest neighbors in the eleven analysed domes. The error bar represents their standard deviations.

that $N_{\rm cells} = A_{\rm ROI}/A_{\rm cell} = R^2\Delta\Omega/A_{\rm cell}$. Thus

$$Q \approx \left(\frac{A_{\rm cell}}{R^2}\right) N_{\rm cells} \ . \tag{2}$$

Fig. 2C shows instead the probability distribution of the number of sides c_i of the cells in the ROI obtained from a sample of eleven domes. We see that a large majority of the cells are either pentagonal or hexagonal with almost half of the observed population being pentagonal (probability of 0.42 ± 0.09 (mean $\pm$ standard deviation)). Since, defects larger than $6-$fold cells are underrepresented this leads to all the domes observed having a positive total topological charge.

III. FORCE BALANCE

In general, the force balance on the surface is given by $\nabla_i \boldsymbol{\sigma}^i = -\boldsymbol{\Xi}^{\rm ext}$ [28, 41],where $\boldsymbol{\sigma}^i$ denotes the surface stress and $\boldsymbol{\Xi}^{\rm ext}$ external forces applied to the system. We use bold letters to refer to vectors in $\mathbb{R}^3$ and latin indices to refer to surface coordinates on $\mathcal{M}$. For example, the stress tensor can be written as a 2×3 matrix. It is possible to decompose the stress into its tangential and normal component, $\boldsymbol{\sigma}^i = \sigma^{ij}\boldsymbol{e}_j + \sigma^i_{\rm n}\boldsymbol{n}$. In the absence of external forces, the force balance can then be written as

$$\nabla_i \boldsymbol{\sigma}^i = \left(\nabla_i \sigma^{ij} + K_i{}^j \sigma^i_n\right) \boldsymbol{e}_j + \left(\nabla_i \sigma^i_n - \sigma^{ij} K_{ij}\right) \boldsymbol{n} = 0 \ . \tag{3}$$

Here, we used $\nabla_i \boldsymbol{n} = K_i{}^j \boldsymbol{e}_j$ and $\nabla_j \boldsymbol{e}_j = -K_{ij}\boldsymbol{n}$. From the free energy of the main text we find, following Ref. [29, 38–40] the tangential and normal stress tensors

$$\sigma^F_{ij} = \gamma g_{ij} - \kappa_B H K_{ij} + \kappa_B H^2 g_{ij} + \kappa_F \left[g_{ij}\chi\nabla^2\chi - \chi\nabla_i\nabla_j\chi + \nabla_i\chi\nabla_j\chi\right] \ , \tag{4}$$

and

$$\sigma^F_{n,i} = \kappa_B \nabla_i H + \kappa_F \left[(2H g_i{}^j - 2K_i{}^j)\chi + 2(K_i^j - 2g_i{}^j H)\right] \nabla_j\chi + \kappa_F K_i{}^j \chi \nabla_j \chi \ . \tag{5}$$

To derive the equations in the main text we use the well-known geometric identity $K g_{ij} = 2HK_{ij} - K_{ik}K_j{}^k$ and the commutator $[\nabla_i, \nabla^2]\chi = -K\nabla_i\chi$. Using these together with the other stress tensors presented in the main text, we find the hydrodynamic equation for the momentum density and the normal force balance by projecting the general force balance onto the tangential and normal direction, respectively. We will present a more detailed derivation in a future work.

IV. DERIVATION OF HEIGHT EQUATION

In this section we derive the height equation, Eq. (5) of the main text, from the general equations describing the dynamics of the active surface, Eqs. (2) and (3) of the main text. We work in the Monge gauge where a height field $h(r)$ is defined as described in the main text. A $+1$ defect is at the center of a disk of radius R and we assume that $|\nabla h| \ll 1$. As shown in the main text, we can find the explicit solutions for the velocity and director fields given in Eqs. (4) from the Eqs. (2) of the main text and we are thus now concerned with rewriting Eq. (3) of the main text. In the small-gradient approximation we have $K \approx 0$, $H \approx -\nabla^2 h/2$, and the metric is just the identity such that covariant derivatives are equal to the flat derivatives. It is then straightforward to see that

$$f_{\rm e}^n = -\gamma \nabla^2 h(r) + \frac{\kappa_B}{2} \nabla^4 h(r) \, . \tag{6}$$

Furthermore, using $\chi(r) = -\log r/R$, we find

$$f_{\rm d}^n = \kappa_F \frac{r\partial_r^2 h(r) - \partial_r h(r)}{r^3} \, . \tag{7}$$

Lastly, for the curvature tensor coupled to the hydrodynamic and active stress tensor, we find the following. We have,

$$K_{ij}\sigma^{{\rm h},ij} = (\nabla_i \nabla_j h) \left[P_{\rm h} \delta^{ij} - \eta \left(\nabla^i v^j + \nabla^j v^i \right) \right] \, , \tag{8}$$

and

$$K_{ij}\sigma^{{\rm a},ij} = \alpha (\nabla_i \nabla_j h) \left(\frac{1}{2} \delta^{ij} - p^i p^j \right) \, , \tag{9}$$

where δ_{ij} is the flat polar metric. For the first term on the right-hand side of both Eq. (8) and Eq. (9) we have $(\nabla^i \nabla^j h)\delta_{ij} = \nabla^2 h$. Furthermore, in polar coordinates $\nabla_i \nabla_j h = \partial_i \partial_j h - \Gamma^k_{ij} \partial_k h$, with Γ^k_{ij} the Christoffel symbol associated with δ_{ij}. This is non-zero only if $i = j = r$, in which case $\nabla_r^2 h = \partial_r^2 h$, or if $i = j = \varphi$, then $\nabla_\varphi^2 h = r\partial_r h$. Similarly, we have $\nabla^i v^j = \partial^i v^j + \delta^{il}\Gamma^j_{kl} v^k$. With $v_r = 0$ and $v_\varphi = v_\varphi(r)$ we then find that this is non-trivial only if $i = r$ and $j = \varphi$ such that $\nabla^r v^\varphi = \partial^r v^\varphi$. Thus, since $\nabla_r \nabla_\varphi h = 0$, the second term in Eq. (8) vanishes. Hence, as mentioned in the main text, the velocity does not enter explicitly in the final equation for h. For the last term we have:

$$p^i p^j \nabla_i \nabla_j h(r) = \cos^2 \epsilon \, \partial_r^2 h(r) + \frac{\sin^2 \epsilon}{r} \partial_r h(r) \, , \tag{10}$$

where $\epsilon = \pm \arccos(-1/\lambda)/2$ as found above. Therefore, adding Eqs. (6)-(9) together, we find

$$0 = f_{\rm e}^n + f_{\rm d}^n + K_{ij} \left(\sigma^{{\rm h},ij} + \sigma^{{\rm a},ij} \right) = \left(P_{\rm h} + \frac{\alpha}{2} - \gamma \right) \nabla^2 h + \frac{\kappa_F}{r} \partial_r \frac{h}{r} + \frac{\lambda - 1}{2\lambda} \partial_r^2 h + \frac{\lambda + 1}{2\lambda r} \partial_r h + \frac{\kappa_B}{2} \nabla^4 h \tag{11}$$

which can be rewritten to yield the height equation, Eq. (5) in the main text.

V. MAPPING TO PHYSICAL UNITS

The model parameters in lattice units used for simulations are $k_\phi = 0.008, A_0 = 0.02, \kappa_F = 0.02, \beta = 0.03, M = 0.1, \Gamma = 1, \lambda = 1.1$, and $\eta = 5/3$. By following previous studies [49, 54], an approximate relation between simulation and physical units (for an active gel of cytoskeletal extracts) can be obtained using $L = 1$ μm as the length-scale, $\tau = 10$ ms as the time-scale, and $F = 1000$ nN as the force-scale. A mapping of some relevant quantities is reported in Table I.

VI. MOVIES

Movie 1: 3D dome animation. 3D rotation and reconstruction of the same MDCK GII monolayer as in Fig. 1D of the main text. Double scaling of the z-direction was chosen to ease the visualization of the buckling instability. The color code is as follows. Red: F-actin, green: E-cadherin, blue: nuclei.

Model parameters	Simulation units	Physical units
Shear viscosity, η	5/3	1.67 KPas
Elastic constant, κ_F	0.02	100 nN
Flow-alignment parameter, λ	1.1	dimensionless
Diffusion constant, $D = Ma$	$0.001 - 0.015$	$0.0087 - 0.0128\ \mu\text{m}^2\text{s}^{-1}$
Activity, α	$0 - 0.01$	$(0 - 100)$ KPa

Table I. Mapping of some relevant quantities between simulation units and physical units.

Movie 2: Profile and tessellation. Left: top-to-bottom confocal z-stack of the same MDCK GII monolayer as in Fig.1D of the main text. At a distance of 15.3 μm to the coverslip, cells are segmented and correlated according to their number of nearest neighbors. Top-right: cross section of the dome. The white lines indicate the inner, middle and outer area of the monolayer. Bottom-right: height-to-radius profile of the buckled monolayer starting from the center of the dome (see also Fig. 1). The position (red circle) follows a sigmoidal fit of the outer area and moves according to the z-stack animation in the left panel. Red: F-actin, green: E-cadherin, blue: nuclei.

Movie 3: Oscillation between buckled states. Oscillations between a cuspidal configuration with negative curvature at the center and a smooth configuration. From an initially flat state the interface buckles. Note that while the initial protrusion is growing the defect is slightly off-center, leading to the whole protrusion moving on the xy-plane. (The z-direction corresponds to the interface normal in the initial state.) After some time ($t > 380000$) the interface starts to periodically oscillate between these two configurations. The oscillation is accompanied by the growth and shrinking of additional thin protrusions at the top. The white vectors denote the polarization field, while the color code refers to the local magnitude of the flow according to the color bar on the right-hand side.

Movie 4: Droplet nucleation. The large extensile active stresses lead to the rapid growth of protrusions that cannot be counteracted by the elasticity of the interface. This results in a periodic breaking of the interface and the consequent nucleation of a droplet after each rupture. There are two +1 defects in the polarization field on each of the droplets. These deform under the straining action of the active liquid crystal on the surface and eventually dissolve due to Ostwald ripening. The white vectors denote the polarization field, while the color code refers to the local magnitude of the flow according to the color bar on the right-hand side.

Movie 5: Chaotic dynamics. Shown is an example of the chaotic dynamics found at very high activity. The complex dynamics in this regime are characterized by chaotic deformations of the membrane with the consequent proliferation of many protrusions at the membrane. The active stresses cannot overcome the elastic forces of the interface and the protrusions break off from the membrane and elongate under the straining effect of bending deformations in the polarization pattern. The white vectors denote the polarization field, while the color code refers to the local magnitude of the flow according to the color bar on the left-hand side.